Received: 25 January 2021 | Revised: 24 February 2021 | Accepted: 25 February 2021

IET Microwaves, Antennas & Propagation

DOI: 10.1049/mia2.12106

The Institution of Engineering and Technology WILEY

ORIGINAL RESEARCH PAPER

Plane wave scattering from thin dielectric disk in free space: Generalized boundary conditions, regularizing Galerkin technique and whispering gallery mode resonances

Mario Lucido[1] | **Mykhaylo V. Balaban**[2] | **Alexander I. Nosich**[2]

[1]Department of Electrical and Information Engineering, University of Cassino and Southern Lazio, Cassino, Italy

[2]Laboratory of Micro and Nano Optics, Institute of Radio-Physics and Electronics NASU, Kharkiv, Ukraine

Correspondence

MarioLucido, Department of Electrical and Information Engineering, University of Cassino and Southern Lazio, Via G. Di Biasio 43, 03043, Cassino, Italy.

Email: lucido@unicas.it

Funding information

MUR, Italian Ministry of University, Grant/Award Number: Dipartimenti di Eccellenza 2018-2022; National Research Foundation of Ukraine, Grant/Award Number: 02-2020-0150

Abstract

Considered is the plane-wave scattering from and absorption by a thin circular dielectric disk. The analysis uses a set of the singular integral equations for the effective electric and magnetic currents, derived using the generalized boundary conditions on the disk median section. Following the recently developed analytical preconditioning procedure, these equations are discretized by the Galerkin technique with judiciously chosen expansion functions, which provide for the Fredholm second-kind nature of the resulting matrix equations. This guarantees the code convergence and high efficiency. It is demonstrated that the developed technique delivers the most important features of thin dielectric disks–the resonances on the natural modes. In the resonances on the slab modes, the disk can be well-transparent and the shadow is created only by its rim; in the whispering gallery mode resonances, the scattering occurs mainly in the disk plane.

1 | INTRODUCTION

Thin flat dielectric disk is a frequently met element of many electromagnetic wave devices across wide spectrum of frequencies and applications. Many of them, if not all, are tied to the fact that such a disk is an open resonator, which is able to support rather high-Q natural modes. If the disk is illuminated with a plane wave or excited by another type of source, then the total field in the near and far zone can display sharp resonances at the natural mode frequencies. For instance, these resonances can be seen as peaks of the total scattering cross-section (TSCS), bistatic radar cross-section (BRCS) in some specific directions, and, in the case of lossy disk material, absorption cross-section (ACS). Lower-order mode resonances are exploited in the dielectric disk microwave antennas and filters [1]. However, even more famous are high-Q resonances associated with the so-called whispering gallery modes (WGMs), supported by disks with larger than wavelength radii. In the millimetre wave range, such disks serve as sensors of host medium refractive index [2] and stabilize the operation of solid state oscillators [3]. The sensing extends to the terahertz, infrared and visible light ranges. Additionally, here a brighter application area thrives: thinner than wavelength disks, grown with molecular beam epitaxy and finely shaped with wet and dry etching are exploited as microlaser cavities [4–7]. They have active regions in the form of a few nanometre thick layers of active materials and their working modes are WGMs. This provides ultra-low thresholds of light emission of such lasers.

Nanotechnologies are expensive, and therefore the preceding modelling with the aid of trusted, accurate and time-economic software becomes not only a desired but also a necessary element of research and development. However, a circular dielectric disk is a truly three-dimensional (3-D) configuration and the electromagnetic wave characterization of such disk calls for a 3-D boundary value problem for the set of Maxwell equations with tangential component continuity conditions, edge condition and radiation condition at infinity.

If the disk has finite thickness, this is a rather complicated vector problem. Reducing it to a guaranteed convergence discretized form can be done using a set of four coupled

Muller boundary integral equations (IEs) [8] and needs smooth enough parameterisation of the disk surface. It is also possible to view the disk as a pillow box with, say, polygonal cross-section and follows ideas of [9], however, the number of coupled IEs increases to 12. Exploitation of rotational symmetry, via expanding the field in terms of the azimuthal Fourier series, brings only a partial alleviation.

Looking for a reasonable simplification of thin disk scatterers, researchers frequently resort to the so-called 'effective refractive index model'. It replaces the 3-D field problem with two simpler ones: a 1-D problem for determining the effective refractive index ν_{eff} and a 2-D problem in the disk plane, that is for a circle filled with material with ν_{eff} instead of $\nu = \varepsilon$, in the free space. As discussed in [10], such a replacement is empiric and fails to characterize the field behaviour off the disk plane completely. Even in that plane, the far field appears as a cylindrical wave instead of the spherical wave as in the original 3-D problem.

As an alternative way of reducing the complexity while keeping the 3-D treatment, in [11] it was proposed to shrink the disk thickness to zero and use so-called generalized (or effective) boundary conditions (GBC), supplemented with the edge condition. The GBC are two-sided conditions; they link together the limiting values of the tangential field components on two 'faces' of thin disk [12, 13]. In this way, the field inside the disk is eliminated from consideration, however, the disk thickness and material constants are still present–they enter the GBC coefficients. This model was further cast to a set of dual IEs in the Hankel transform domain that was reduced to the coupled Fredholm second-kind IEs. This guaranteed the convergence of numerical solution; short study of a disk excited by on-axis parallel-oriented elementary dipole was presented in [14]. Note that the median line IE, obtained from GBC, can be also solved using Nystrom discretization, which guarantees convergence as well; this was done in [15] for a 2-D material strip scattering. It should be also noted that validity and limitations of GBC model, with respect to 'thick' strip analysis using the Muller IEs, were established in [16].

On adopting such a model, one can easily see that its accurate treatment has much in common with canonical scattering problems associated with zero-thickness perfect electric conducting (PEC) planar scatterers [17]. PEC disk scattering has been attacked by many techniques. Their comprehensive review can be found in [18–21] and therefore is not given here. Still, we believe that the most efficient technique for studying a PEC disk, with guaranteed convergence, is the technique developed in [19]. This is a version of the Galerkin MoM combined with the Helmholtz decomposition, which was initially applied, in the full form, to the analysis of the plane wave scattering from a hollow finite length PEC circular cylinder [22] and, in the simplest form, to the analysis of axially symmetric circular dielectric disk antennas [23]. Here, the basis functions are orthogonal eigenfunctions of the static limit of the corresponding spatial hypersingular IE, hence, that IE is converted directly into a Fredholm second-kind matrix equation.

In [24], this efficient technique was applied to the analysis of the plane wave scattering from a resistive disk. In the current work, we apply it, with necessary modifications done in [25], to the analysis of plane wave scattering and absorption by a thin dielectric high contrast disk. So far, only a preliminary study of the convergence of the method has been performed by the authors [25]. The focus of our analysis is the most important for applications question of the resonances on the disk natural modes. This includes two types of modes. One is related to the modes of infinite dielectric slab, which, in perturbed form, exists on finite disk as well. We call them slab modes or transverse modes. The other type corresponds to the in-plane modes, which include WGMs. We explore whether the WGM effect can be characterized properly, despite the use of GBC and median line IEs.

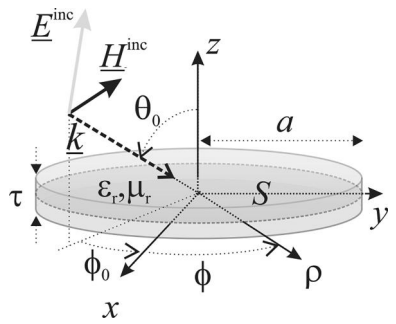

FIGURE 1 Geometry of the problem

The remainder of this study is as follows. In Section 2, an overview of the formulation of the problem and the proposed solution is briefly presented. In Section 3, the far field parameters used to search for the disk resonances are described. Section 4 is devoted to show the obtained numerical results. The conclusions are summarized in Section 5, and two Appendices conclude the study.

2 | BACKGROUND: FORMULATION OF THE PROBLEM AND REGULARIZING DISCRETIZATION SCHEME

Thin magneto-dielectric disk of radius a, thickness τ, dielectric permittivity $\varepsilon = \varepsilon_0\varepsilon_r$ and magnetic permeability $\mu = \mu_0\mu_r$ immersed in free space (of material constants ε_0 and μ_0) and coaxial with disk cylindrical coordinate system (ρ, ϕ, z) with the origin at the centre of the disk are sketched in Figure 1. Let us denote with λ - the free-space wavelength, with ω - the angular frequency and with $k_0 = 2\pi/\lambda = \omega\sqrt{\epsilon_0\mu_0}$- the free-space wavenumber.

A plane wave with $\underline{E}^{\text{inc}}(\underline{r}) = \underline{E}_0 e^{-j\underline{k}\cdot\underline{r}}$ and $\underline{H}^{\text{inc}}(\underline{r}) = \underline{H}_0 e^{-j\underline{k}\cdot\underline{r}} = \hat{k} \times \underline{E}_0 e^{-j\underline{k}\cdot\underline{r}}/Z_0$, where $\underline{r} = (\rho, \phi, z)$, $\underline{k} = -k_0(\sin\theta_0\cos(\phi_0 - \phi)\hat{\rho} + \sin\theta_0 \sin(\phi_0 - \phi)\hat{\phi} + \cos\theta_0\hat{z})$ and $Z_0 = \sqrt{\mu_0/\varepsilon_0}$, impinges onto the disk such that a scattered field, $(\underline{E}^{\text{sc}}(\underline{r}), \underline{H}^{\text{sc}}(\underline{r}))$, arises. Moreover, the total field, $(\underline{E}(\underline{r}), \underline{H}(\underline{r}))$, is given by the sum of the incident field and the scattered field.

Assuming that $\tau = \lambda$ and $\tau = a$, the field inside the disk can be neglected and the disk approximated with a flat

zero-thickness median surface, S, located at $z = 0$ for $\rho \leq a$ and $\phi \in [0, 2\pi]$, on which the following GBC have to be satisfied [12, 13, 25]:

$$\frac{1}{2}\hat{z} \times (\underline{E}(\rho, \phi, 0^+) + \underline{E}(\rho, \phi, 0^-)) \times \hat{z} = R_e \underline{J}_e(\rho, \phi) \quad (1a)$$

$$\frac{1}{2}\hat{z} \times (\underline{H}(\rho, \phi, 0^+) + \underline{H}(\rho, \phi, 0^-)) \times \hat{z} = R_m \underline{J}_m(\rho, \phi) \quad (1b)$$

where the currents are the field jumps across S,

$$\underline{J}_e(\rho, \phi) = \hat{z} \times \left(\underline{H}^{sc}(\rho, \phi, 0^+) - \underline{H}^{sc}(\rho, \phi, 0^-)\right) \quad (2a)$$

$$\underline{J}_m(\rho, \phi) = -\hat{z} \times \left(\underline{E}^{sc}(\rho, \phi, 0^+) - \underline{E}^{sc}(\rho, \phi, 0^-)\right) \quad (2b)$$

If the disk material is high contrast, $|\varepsilon_r \mu_r| \gg 1$, then the electric and magnetic resistivities are, respectively,

$$R_e = -\mathrm{j}\, Z \cot\left(\frac{1}{2} k_0 \sqrt{\varepsilon_r \mu_r}\, \tau\right) \quad (3a)$$

$$R_m = -\mathrm{j}\, Z^{-1} \cot\left(\frac{1}{2} k_0 \sqrt{\varepsilon_r \mu_r}\, \tau\right) \quad (3b)$$

where $Z = \sqrt{\mu/\varepsilon}$ is the material impedance [12].

The problem at hand is a boundary value problem for the Maxwell equations, which is uniquely solvable provided that boundary conditions, edge condition (or, equivalently, local power boundedness condition) and Silver–Muller radiation condition are satisfied [26, 27].

The field, scattered from the disk, can be sought for in the form of convolutions of the unknown effective electric and magnetic current densities with the Green's functions and their normal to disk derivatives. On substitution into GBC Equation (1) on S, two decoupled surface IEs for the effective currents can be readily obtained [12]. Taking advantage of the revolution symmetry of the problem, these equations can be reduced to two infinite sets of independent one-dimensional IEs in the Hankel transform domain [25]:

$$\int_0^{+\infty} \underline{\underline{\mathbf{H}}}^{(n)}(w\rho) \left[\underline{\underline{\tilde{\mathbf{G}}}}_r(w) - R_r \underline{\underline{I}}\right] \underline{\tilde{\mathbf{J}}}_r^{(n)}(w) w dw = -\underline{\mathbf{F}}_r^{\mathrm{inc}(n)}(\rho, 0) \quad (4)$$

for $\rho \leq a$ and with $r = \mathrm{e}, \mathrm{m}$, $F_e = E$ and $F_m = H$, where the apex n denotes the n-th term of the Fourier series, the symbol

$$\underline{\mathbf{P}}^{(n)}(\cdot) = \begin{pmatrix} P_\rho^{(n)}(\cdot) \\ -\mathrm{j}\, P_\phi^{(n)}(\cdot) \end{pmatrix} \quad (5)$$

has been introduced,

$$\underline{\tilde{\mathbf{J}}}_r^{(n)}(w) = \int_0^{+\infty} \underline{\underline{\mathbf{H}}}^{(n)}(w\rho) \underline{\mathbf{J}}_r^{(n)}(\rho) \rho d\rho \quad (6)$$

are the vector Hankel transform of order n (VHT$_n$) of the n-th harmonics of the electric and magnetic currents,

$$\underline{\underline{\mathbf{H}}}^{(n)}(w\rho) = \begin{pmatrix} J'_n(w\rho) & nJ_n(w\rho)/(w\rho) \\ nJ_n(w\rho)/(w\rho) & J'_n(w\rho) \end{pmatrix} \quad (7)$$

$J_n(\cdot)$ and $J'_n(\cdot)$ are the Bessel function of the first kind and order n and its first derivative with respect to the argument, respectively [28],

$$\underline{\underline{\tilde{\mathbf{G}}}}_r(w) = \begin{pmatrix} \tilde{G}_{r,\mathrm{C}}(w) & 0 \\ 0 & \tilde{G}_{r,\mathrm{D}}(w) \end{pmatrix} = \\ = \frac{1}{2\omega\eta_r} \begin{pmatrix} -\sqrt{k_0^2 - w^2} & 0 \\ 0 & -k_0^2 \Big/ \sqrt{k_0^2 - w^2} \end{pmatrix} \quad (8)$$

$\eta_e = \varepsilon_0$, $\eta_m = \mu_0$ and $\sqrt{k_0^2 - w^2} = -\mathrm{j}\sqrt{-k_0^2 + w^2}$.

Equation (4) can only be solved by making use of numerical techniques. To this purpose, it is more advisable to handle with scalar unknowns instead of vector ones. The Helmholtz decomposition of the unknowns, that is,

$$\underline{\mathbf{J}}_r^{(n)}(\rho) = \underbrace{\begin{pmatrix} \frac{d}{d\rho} \\ \frac{n}{\rho} \end{pmatrix} \Phi_{r,\mathrm{C}}^{(n)}(\rho)}_{\underline{\mathbf{J}}_{r,\mathrm{C}}^{(n)}(\rho)} \underbrace{-\mathrm{j} \begin{pmatrix} \frac{n}{\rho} \\ \frac{d}{d\rho} \end{pmatrix} \Phi_{r,\mathrm{D}}^{(n)}(\rho)}_{\underline{\mathbf{J}}_{r,\mathrm{D}}^{(n)}(\rho)} \quad (9)$$

where the functions $\Phi_{r,T}^{(n)}(\rho)$ for $T = \mathrm{C}, \mathrm{D}$ are suitable potential functions [29], and the subscripts C and D denote the surface curl-free and the surface divergence-free contributions of the surface current densities, respectively, can be the appropriate choice because the VHT$_n$ of each contribution has only one nonvanishing component, that is,

$$\underline{\tilde{J}}_r^{(n)}(w) = \underbrace{\begin{pmatrix} \tilde{J}_{r,\mathrm{C}}^{(n)}(w) \\ 0 \end{pmatrix}}_{\underline{\tilde{J}}_{r,\mathrm{C}}^{(n)}(w)} + \underbrace{\begin{pmatrix} 0 \\ -\mathrm{j}\, \tilde{J}_{r,\mathrm{D}}^{(n)}(w) \end{pmatrix}}_{\underline{\tilde{J}}_{r,\mathrm{D}}^{(n)}(w)} \quad (10)$$

The obtained IEs are discretized by means of the Galerkin method. In order to guarantee the convergence, the key point

is the proper selection of the sets of basis functions to be used. Suitable expansion series for the nonvanishing components of the contributions in Equation (10) are shown in the following [19, 24, 25]:

$$\tilde{J}^{(n)}_{r,T}(w) = \sum_{h=-1+\delta_{n,0}}^{+\infty} \gamma^{(n)}_{r,T,h} \tilde{f}^{(n)}_{T,h}(w) \tag{11a}$$

$$\tilde{f}^{(n)}_{T,h}(w) = \sqrt{2\eta^{(n)}_{T,h}} \frac{J_{\eta^{(n)}_{T,h}}(aw)}{w^{p_T}} \tag{11b}$$

$$\eta^{(n)}_{T,h} = |n| + 2h + p_T + 1 \tag{11c}$$

where $\delta_{n,m}$ is the Kronecker delta and $\gamma^{(n)}_{r,T,h}$ denotes the general expansion coefficient, which are complete and nonredundant Neumann series of the weighted Bessel functions, orthonormal on the interval $(0, +\infty)$ with the weight function w^{2p_T-1} [30], and have closed form spatial domain counterparts. With such a choice, the physical behaviour of the components of the cylindrical harmonics of the currents around the centre of the disk is reconstructed. By setting $p_C = 3/2$ and $p_D = 1$, even the edge behaviour of the unknowns is reconstructed and the unique solvability of the general 1-D IE in Equation (4) is guaranteed [24]. Moreover, following the line of reasoning in [19, 24], it is possible to show that the general matrix equation obtained by means of the Galerkin method with the expansion functions Equation (11) (shown in Appendix A for the sake of completeness) is a Fredholm equation of the second kind in l^2 because both the matrix operator and the free term have bounded l^2-norms [19].

3 | FAR FIELD PARAMETERS

Using the stationary phase method, the far electric field can be expressed in closed form [27] as:

$$E^{sc}_s(r,\theta,\phi) \overset{r\to+\infty}{\sim} e^{-j\,k_0 r} r^{-1} F_s(\theta,\phi) \tag{12}$$

with $s = \theta, \phi$, where, in our case:

$$F_\theta(\theta,\phi) = -\frac{k_0}{2} \sum_{n=-\infty}^{+\infty} e^{j\,n\left(\phi+\frac{\pi}{2}\right)} \left(c_\theta Z_0 \tilde{J}^{(n)}_{e,C}(k_0 s_\theta) + \tilde{J}^{(n)}_{m,D}(k_0 s_\theta) \right) \tag{13a}$$

$$F_\phi(\theta,\phi) = -\frac{k_0}{2} \sum_{n=-\infty}^{+\infty} e^{j\,n\left(\phi+\frac{\pi}{2}\right)} \left(Z_0 \tilde{J}^{(n)}_{e,D}(k_0 s_\theta) - c_\theta \tilde{J}^{(n)}_{m,C}(k_0 s_\theta) \right) \tag{13b}$$

$s_\theta = \sin\theta$ and $c_\theta = \cos\theta$. The following expression can be readily written for BRCS:

$$\sigma_{BRCS}(\theta,\phi) = \lim_{r\to+\infty} \frac{4\pi r^2 |\underline{E}^{sc}(r,\theta,\phi)|^2}{\left|\underline{E}^{inc}(r,\theta,\phi)\right|^2} = \frac{4\pi |\underline{F}(\theta,\phi)|^2}{|\underline{E}_0|^2} \tag{14}$$

Moreover, the quantity $\sigma_{BSCS} = \sigma_{BRCS}(\theta_0,\phi_0)$ defines the back scattering cross-section (BSCS) while $\sigma_{FSCS} = \sigma_{BRCS}(\pi - \theta_0, \pi + \phi_0)$ is the forward scattering cross-section (FSCS).

TSCS and ACS are defined as follows:

$$\sigma_{TSCS} = \frac{1}{4\pi} \int_0^\pi \int_0^{2\pi} \sigma_{BRCS}(\theta,\phi) \sin\theta d\phi d\theta = \\ = \frac{1}{|\underline{E}_0|^2} \int_0^\pi \int_0^{2\pi} |\underline{F}(\theta,\phi)|^2 \sin\theta d\phi d\theta \tag{15a}$$

$$\sigma_{ACS} = \frac{P^{abs}}{|\underline{E}_0|^2/(2Z_0)} = \\ = \frac{Z_0}{|\underline{E}_0|^2} \int_0^a \int_0^{2\pi} \left(\Re\{R_e\} |J_e(\rho,\phi)|^2 + \Re\{R_m\} |J_m(\rho,\phi)|^2 \right) \rho d\phi d\rho = \\ = \frac{2\pi Z_0}{|\underline{E}_0|^2} \sum_{n=-\infty}^{+\infty} \int_0^a \left(\Re\{R_e\} \left|\underline{J}^{(n)}_e(\rho)\right|^2 + \Re\{R_m\} \left|\underline{J}^{(n)}_m(\rho)\right|^2 \right) \rho d\rho \tag{15b}$$

where P^{abs} denotes the power absorbed by a lossy disk and $\Re\{\cdot\}$ denotes the real part of a complex number. They are related to each other by means of the forward scattering theorem (also known as optical theorem in optics) [31], that is,

$$\sigma_{TSCS} + \sigma_{ACS} = -\frac{4\pi}{k_0 |\underline{E}_0|^2} \Im\left\{ \underline{E}_0^* \cdot \underline{F}(\pi - \theta_0, \pi + \phi_0) \right\} \tag{16}$$

where $\Im\{\cdot\}$ denotes the imaginary part of a complex number and the star is for the complex conjugate of a complex number. It is interesting to observe that, by means of Parseval equality [32] and the Weber–Schafheitlin discontinuous integral [33], ACS can be expressed in closed form (see Appendix B for the details). Hence, according to Equation (16), even TSCS admits a closed form expression.

To conclude, all the far field parameters detailed above are expressed in closed form. As a result, they are very handy tools for the characterization of the resonances of a dielectric disk.

4 | NUMERICAL RESULTS

This section is aimed at showing that the proposed approach, based on GBC and median-surface IE, allows to fully characterize the physical properties of a thin dielectric disk with $|\varepsilon_r \mu_r| \gg 1$, $\tau \ll a$ and $\tau \ll \lambda$. In order to avoid unnecessary repetitions, it is worth noting that the fast convergence of the method and the correctness of the corresponding software code have been extensively demonstrated in [25] by means of comparisons with the commercial software CST Microwave Studio (CST-MWS). Moreover, it has been convincingly shown in [25] that the proposed method drastically outperforms CST-MWS in terms of both computation time and

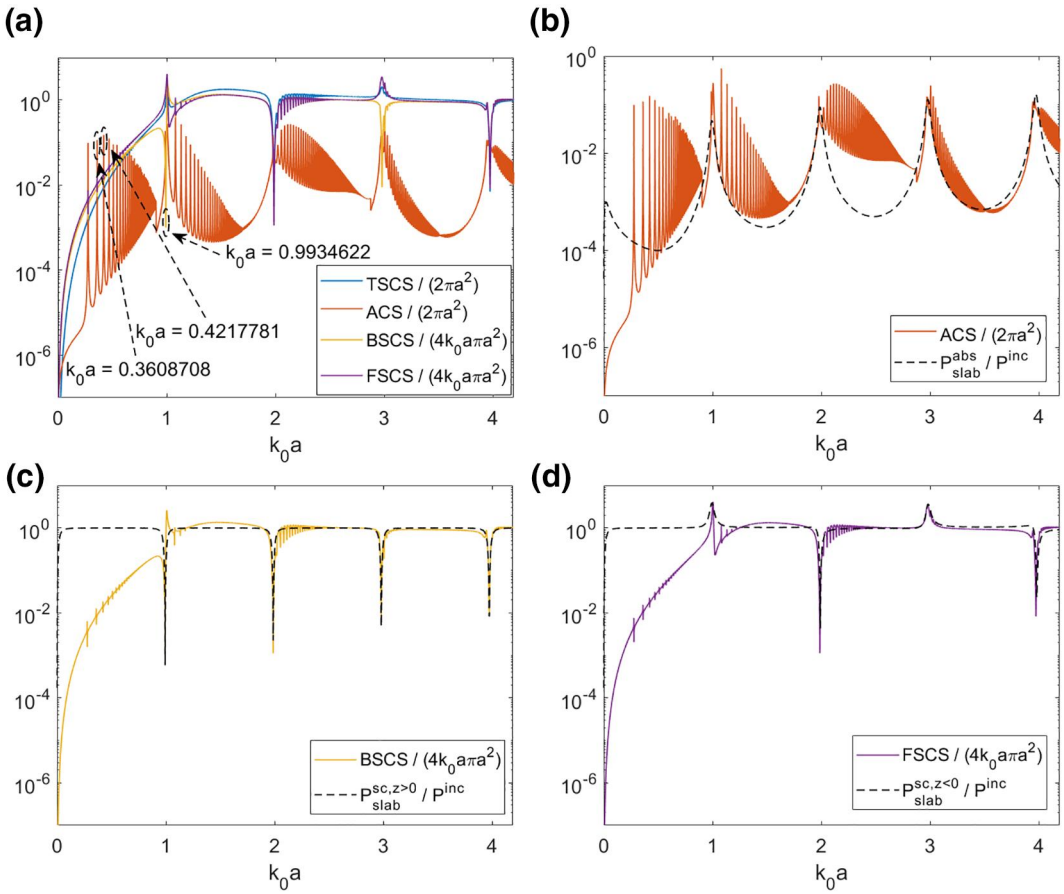

FIGURE 2 Far field parameters of the disk with $\varepsilon_r = 1000-j$, $\mu_r = 1$ and $\tau/a = 0.1$ when a plane wave orthogonally impinges onto the disk ($\theta_0 = 0°$) with $\underline{E}_0 = 1\hat{y}$ V/m for varying values of $k_0 a$, compared with the corresponding parameters of an infinite dielectric slab with the same dielectric permittivity, magnetic permeability and thickness: (a) TSCS, ACS, BSCS and FSCS of the disk, (b) ACS of the disk versus normalized power absorbed by the infinite dielectric slab, (c) BSCS of the disk versus normalized power scattered in the top half-space from the infinite dielectric slab and (d) FSCS of the disk versus normalized power scattered in the bottom half-space from the infinite dielectric slab

storage requirement. As a matter of fact, CST-MWS does not provide a 2-D model for dielectric objects, and an accurate simulation of thin 3-D objects has revealed to be time-consuming and onerous in terms of memory requirements. Regarding the cases examined, CST-MWS simulations would take several hours and tens of millions of mesh-cells to reconstruct the solutions on a PC equipped with an Intel Core i7-10510U 1.8 GHz, 16 GB RAM, running Windows 10. On the other hand, as clearly stated in the following, short computation time and few expansion functions are needed to reconstruct the solutions with the proposed convergent method.

As mentioned above, we assume that $\tau = \lambda$ as a necessary albeit empiric precondition for the use of GBC. However, this condition does not exclude the possibility that the disk thickness is larger than the wavelength in the disk material, that is, $\tau > \lambda/\sqrt{|\varepsilon_r|}$ [12]. For this reason, in order to make an exhaustive analysis of the dielectric disk properties, we will follow [15] and assume $\Re\{\varepsilon_r\} = 1000$. Such a value may seem unusual, however, it can be associated with one of the novel colossal permittivity materials [34]; this allows us to 'catch' a few slab-mode resonances even if $\tau = \lambda$.

In order to quantify the rate of solution convergence, the following normalized truncation error is introduced:

$$\mathrm{err}_{r,N}(M) = \sqrt{\sum_{n=-N+1}^{N-1} \left\| \mathbf{x}_{r,M+1}^{(n)} - \mathbf{x}_{r,M}^{(n)} \right\|^2 \Bigg/ \sum_{n=-N+1}^{N-1} \left\| \mathbf{x}_{r,M}^{(n)} \right\|^2} \tag{17}$$

where $2N-1$ is the number of the considered harmonics estimated as in [35], $\|\cdot\|$ is the usual Euclidean norm and $x_{r,M}^{(n)}$ is the vector of all expansion coefficients of the n-th harmonic (see (A2b), (A2m) and (A2n)) evaluated using M expansion functions for each unknown. Since, according to the Fredholm theory, $\lim_{M\to+\infty} \mathrm{err}_{r,N}(M) = 0$, henceforth, M is chosen in order to guarantee that both $\mathrm{err}_{c,N}(M)$ and $\mathrm{err}_{m,N}(M)$ are below 10^{-2}. It is worth noting that, generally, this value is moderately larger if the error of less than 10^{-3} is desired. As known, the error in the far field characteristics is by order of magnitude smaller.

Figure 2(a) shows the behaviour of TSCS, ACS, BSCS and FSCS of the disk with $\varepsilon_r = 1000-j$, $\mu_r = 1$ and $\tau/a = 0.1$ if a

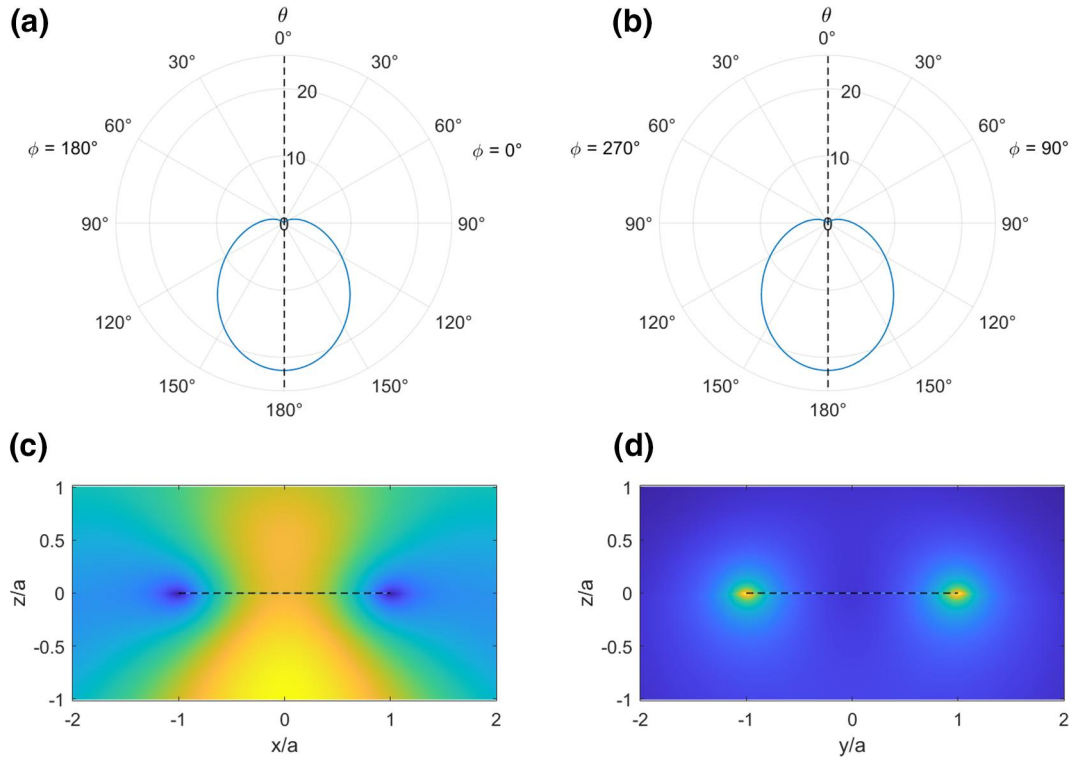

FIGURE 3 BRCS and near E-field behaviour of the disk with $\varepsilon_r = 1000-j$, $\mu_r = 1$ and $\tau/a = 0.1$ when a plane wave orthogonally impinges onto the disk ($\theta_0 = 0°$) with $\underline{E}_0 = 1\hat{y}$ V/m at the transverse resonance frequency $k_0 a = 0.9934622$: (a) BRCS in the *xz*-plane, (b) BRCS in the *yz*-plane, (c) near E-field in the *xz*-plane and (d) near E-field in the *yz*-plane

plane wave orthogonally impinges onto the disk ($\theta_0 = 0°$) with $\underline{E}_0 = 1\hat{y}$ V/m, for varying values of $k_0 a$. In that case, only the harmonics for $n = \pm 1$ contribute to the field's representation.

The most pronounced minima of BSCS, which can be observed for $k_0\sqrt{|\varepsilon_r|}\tau \cong n\pi$ with $n = 1,2,...$, are associated with the slab modes, also called transverse resonance modes. This conclusion is simply justified in Figure 2(c) by comparing BSCS of the disk with the power scattered into the upper half-space from an infinite dielectric slab of the same material and thickness as the disk normalized to the incident power ($P_{slab}^{sc,z>0}/P^{inc}$). Moreover, as shown in Figure 2(d), even FSCS and the normalized power scattered from the dielectric slab into the lower half-space ($P_{slab}^{sc,z<0}/P^{inc}$) have the same behaviour around the slab mode resonance frequencies. BRCS and the near E-field pattern at the normalized slab mode resonance frequency, $k_0 a = 0.9934622$, at which $M = 6$ and a computation time less than 1 s are enough to accurately reconstruct the solution, are shown in Figure 3. As can be clearly seen, a substantial transparency is observed so that the shadow is produced by the disk rim only. These slab modes can be denoted as S_n, $n = 1, 2, \ldots$. Note that the interchanging maxima and minima of TSCS are explained by the symmetry or antisymmetry of the eigenfield of the corresponding slab mode relatively to the median line.

The plots of ACS in Figure 2(b) show numerous peaks, which are not reflected in the normalized power absorbed by the infinite dielectric slab (P_{slab}^{abs}/P^{inc}). At the normal incidence of a plane wave, all of them are associated with the 'dipole-type' disk modes having the azimuthal index $n = 1$ and the radial indices $m = 1, 2, \ldots$. Two examples of the near E-field of such kind of modes are shown: for $H_{2,1,0}$ at $k_0 a = 0.3608708$ and $H_{3,1,0}$ at $k_0 a = 0.4217781$ in Figure 4(a) and 5(c) and in Figure 4(b) and 4(d), respectively. Here, the first subscript takes into account the radial variation of the field, while the second one and third one stand for the azimuthal and transversal variations, respectively. As expected, the near E-field behaviour shows the hot spots stretched only along the *x*-axis. It is worth noting that, for the two examples considered, the solutions are accurately (i.e. with error in Equation (17) less than 10^{-2}) reconstructed by selecting $M = 7$ and $M = 8$, respectively, with a computation time of about 1 s.

Figure 5(a) shows TSCS, ACS, BSCS and FSCS for a TE polarized plane wave impinging onto the disk with $|\underline{E}_0| = 1$ V/m, $\theta_0 = 0°$, 45° ,90° and $\phi_0 = 0°$, for varying values of $k_0 a$. As can be clearly seen, new peaks arise (emphasized by the straight *dotted lines*) for oblique incidence. This is because now, in the scattered field, all azimuthal harmonics are involved including the 0-th one. Figure 5(b) and (d) shows the near E-field at $k_0 a = 0.3269092$ for $\theta_0 = 45°$ while in Figure 5(c) and (e), the near E-field at $k_0 a = 0.3952056$ for $\theta_0 = 90°$is plotted. In either case, the considered resonance modes are identified as axially symmetrical modes $H_{2,0,0}$ and $H_{3,0,0}$; their frequencies are almost independent of the incidence angle. As the cases examined above, the solutions are

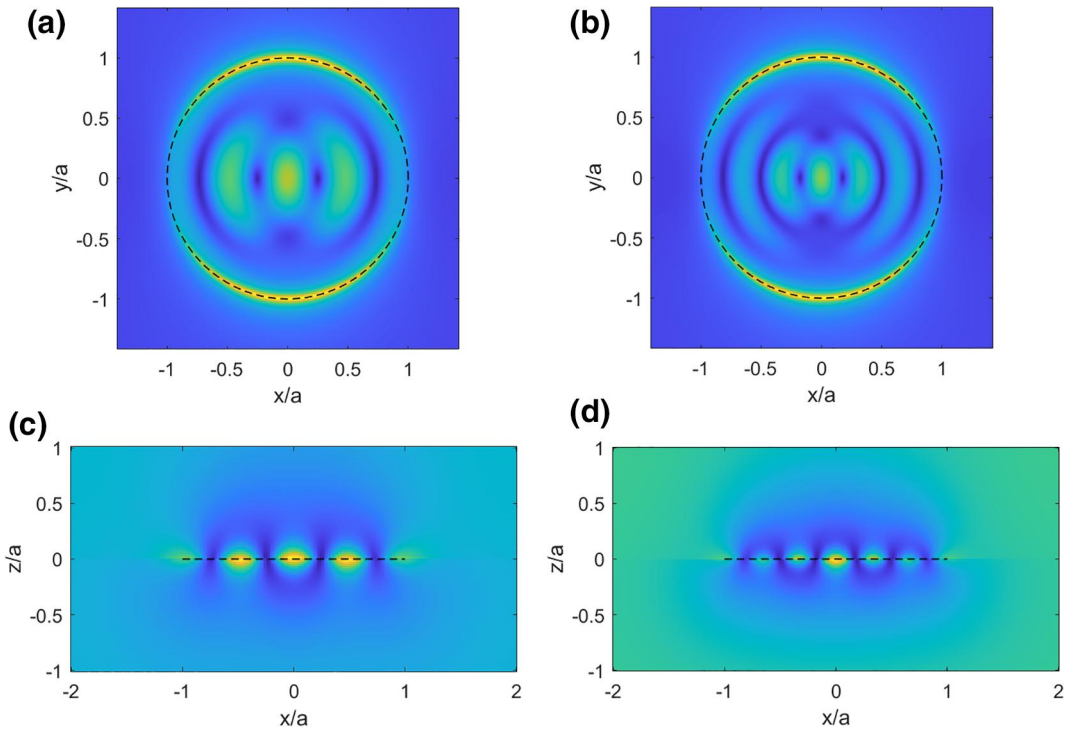

FIGURE 4 Near E-field behaviour in the *xy*- and *xz*-planes of the disk with $\varepsilon_r = 1000-j$, $\mu_r = 1$ and $\tau/a = 0.1$ when a plane wave orthogonally impinges onto the disk ($\theta_0 = 0°$) with $\underline{E}_0 = 1\hat{y}$ V/m at dipole mode resonance frequencies: (a) near E-field in the *xy*-plane for $k_0a = 0.3608708$ ($H_{2,1,0}$), (b) near E-field in the *xy*-plane for $k_0a = 0.4217781$($H_{3,1,0}$), (c) near E-field in the *xz*-plane for $k_0a = 0.3608708$ ($H_{2,1,0}$) and (d) near E-field in the *xz*-plane for $k_0a = 0.4217781$ ($H_{3,1,0}$)

accurately reconstructed by choosing $M = 7$ and $M = 8$, respectively, even if now $N = 4$ has to be considered, with a computation time of about 1.5 s. It is interesting to observe that all the new resonances arising for oblique incidence shown in Figure 5(a) are associated to axially symmetrical modes, while the 'dipole-mode' resonances are present both in the normal and inclined incidence cases. Note that just above, in frequency, of the first slab mode resonance, new sequence of in-plane mode resonances appears. These new modes have their fields with one variation along the *z*-axis, hence their third index, $q = 1$.

Naturally, a question arises about the resonances on the higher azimuthal harmonics, including WGMs, which must also give response to the plane wave excitation at the inclined incidence.

To provide the conditions for sufficiently high Q-factors of WGMs, we assume now that the losses in material are two orders lower than in the case examined in Figures 2–5, $\varepsilon_r = 1000-j\,10^{-2}$. Moreover, in order to maximize the number of significant harmonics of the incident field, the grazing incidence is considered.

For the TE polarization, the behaviour of TSCS, ACS, BSCS and FSCS versus the normalized frequency is shown in Figure 6(a). One can clearly see an almost periodic sequence of sharp peaks associated with principal WGMs of the radial index $n = 1$ and azimuthal indices $m = 2, 3, \ldots$ Their analysis demonstrates that while ACS reaches maximum values at all WGM frequencies, and TSCS–at least at all higher-m WGMs, both the FSCS and especially BSCS can drop sharply. The explanation is, apparently, in the fact that the eigenfields of each WGM have $2m$ identical intensive lobes, radiating in the disk plane only. Thus, at the grazing incidence, 'ignition' of such a field spoils mainly the backward scattering while the forward scattering, dominated by the shadow lobe, is less vulnerable.

In Figure 6(b) and (d), the near E-field behaviour of the $WGMH_{1,3,2}$ can be observed at $k_0a = 2.0467460$, while the near E-field behaviour of the $WGMH_{1,4,2}$, obtained at $k_0a = 2.0590945$, is shown in Figure 6(c) and (e). Here, the third index is $q = 2$ because their frequencies are above the second slab mode, S_2 – see Figure 2. It is interesting to note that, besides the classical 'necklace' pattern of the field hot spots, known for 2-D circular cavity, a bright edge can be observed due to the singular edge behaviour in the zero-thickness GBC model considered. This feature, which is natural in the 3-D modelling, cannot be reproduced in the 2-D modelling with the aid of empiric 'effective refractive index' concept. It is interesting to observe that, even in such cases, few expansion functions, $M = 24$ and $M = 23$, respectively, and harmonics, $N = 9$, are needed to obtain the solutions within less than 10^{-2} error in Equation (17) with a computation time of only 8 s.

Far field patterns in the *xy*-plane at the same resonance frequencies are shown in Figure 6(f) and 6(g), respectively. They show the shadow lobes in the forward direction and intensive sidelobes appearing around the disk.

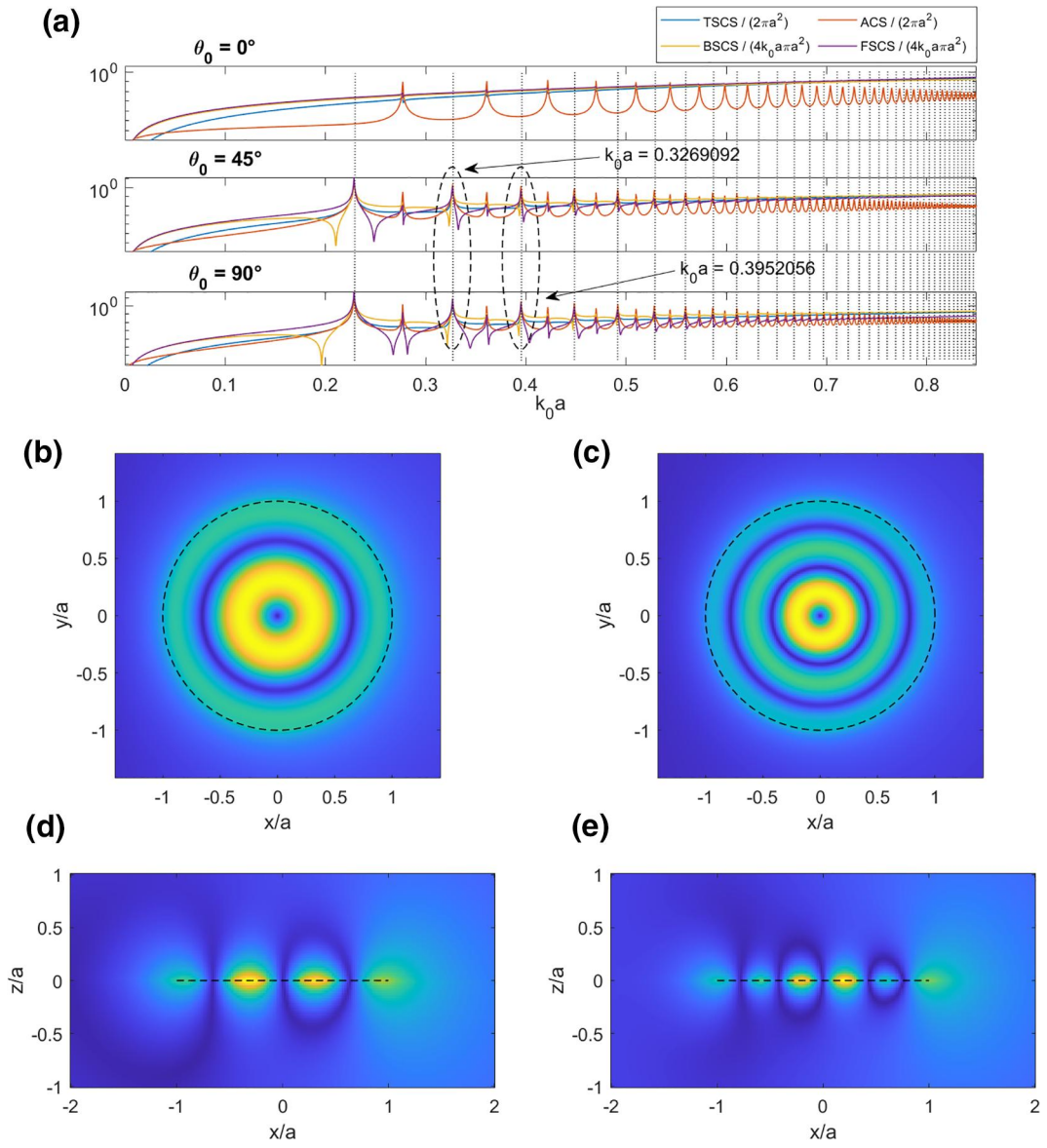

FIGURE 5 Far field parameters for varying values of k_0a and near E-field behaviour in the *xy*- and *xz*-planes at the axially symmetrical resonance frequencies of the disk with $\varepsilon_r = 1000-j$, $\mu_r = 1$, $\tau/a = 0.1$ when a TE polarized plane wave with $|\underline{E}_0| = 1$ V/m and $\phi_0 = 0°$ obliquely impinges onto the disk: (a) TSCS, ACS, BSCS and FSCS for $\theta_0 = 0°$, 45°, 90° and varying values of k_0a, (b) near E-field in the *xy*-plane for $k_0a = 0.3269092$ and $\theta_0 = 45°$ ($H_{2,0,0}$), (c) near E-field in the *xy*-plane for $k_0a = 0.3952056$ and $\theta_0 = 90°$ ($H_{3,0,0}$), (d) near E-field in the *xz*-plane for $k_0a = 0.3269092$ and $\theta_0 = 45°$ ($H_{2,0,0}$) and (e) near E-field in the *xz*-plane for $k_0a = 0.3952056$ and $\theta_0 = 90°$ ($H_{3,0,0}$)

5 | CONCLUSION

We have presented the essentials of the MAR-based computational technique and analysis results for the plane wave scattering from and absorption by a thin circular dielectric disk. Thanks to the judiciously chosen expansion functions in the Galerkin MoM discretization of associates singular IEs, we can exploit all the power of the Fredholm second-kind matrix equations and enjoy the guaranteed convergence.

The main objective of our study has been the verification of whether or not the use of GBC and zero-thickness 'effective' disk model can deliver the practically important effect of the natural mode resonances. We have demonstrated that this is true: as we have found, in the resonances on the slab modes, the disk can be well-transparent and the shadow is created only by its rim; in the WGM resonances, the near-field pattern is dominated with characteristic azimuthally periodic 'necklace' of the field hot spots and the scattering occurs mainly in the disk plane. Interestingly, the considered model, despite being simplified because the field inside the disk is ignored, is still able to reproduce the field variations, at higher frequencies, along the disk axis. This feature is incorporated into GBC, which are, therefore, applicable in wider range of parameters than could be expected. Another feature, which is well reproduced, is the singular behaviour of some of the field components near the rim of 3-D dielectric disk.

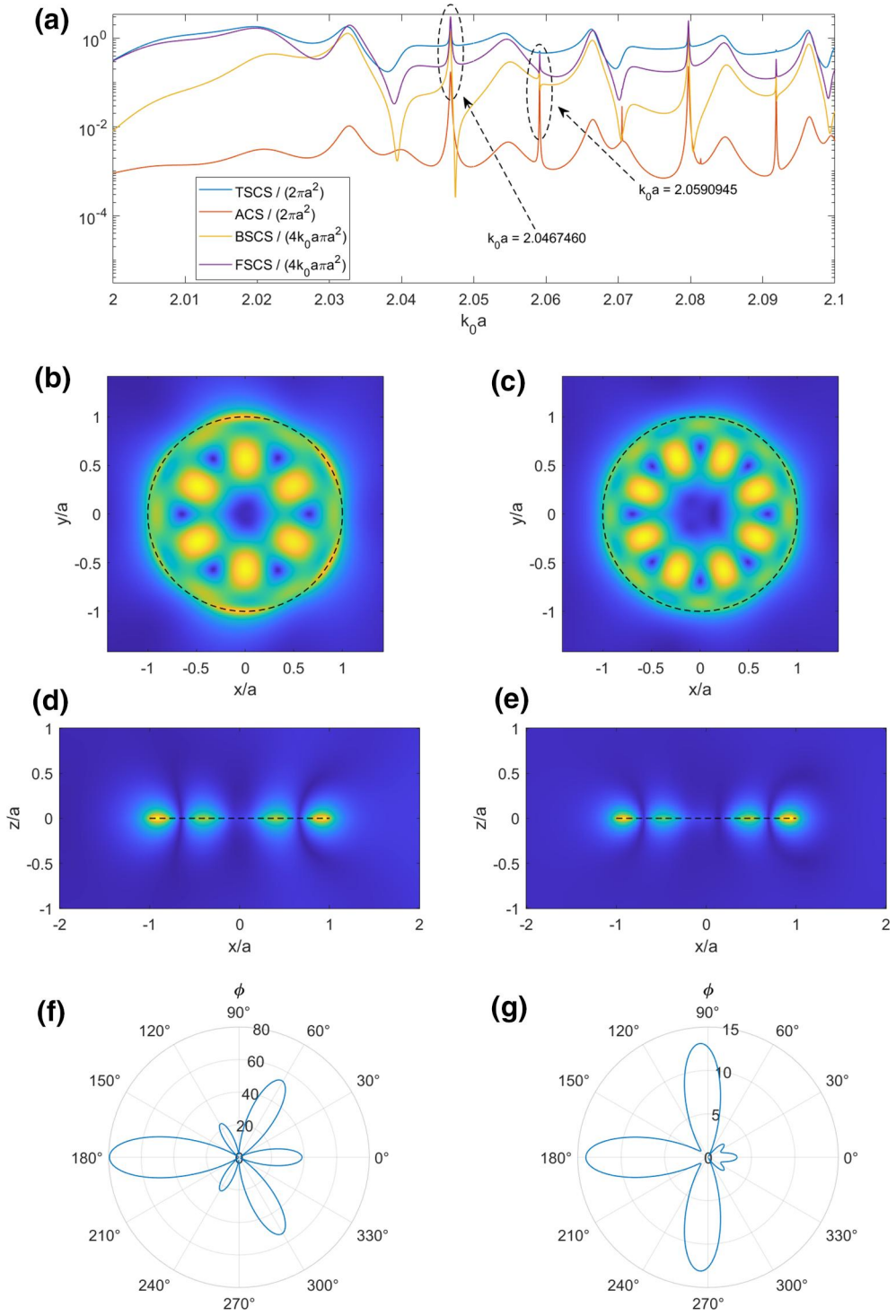

FIGURE 6 Far field parameters for varying values of k_0a, near E-field behaviour in the *xy*- and *xz*-planes, and BRCS in the *xy*-plane at the WGMs resonance frequencies of a disk with $\varepsilon_r = 1000 - j\,10^{-2}$, $\mu_r = 1$, $\tau/a = 0.1$ when a TE polarized plane wave with $|\underline{E}_0| = 1$ V/m and $\phi_0 = 0°$ impinges onto the disk at the grazing incidence: (a) TSCS, ACS, BSCS and FSCS for varying values of k_0a, (b) near E-field for $k_0a = 2.0467460$ in the *xy*-plane ($WGMH_{1,3,2}$), (c) near E-field for $k_0a = 2.0590945$ in the *xy*-plane ($WGMH_{1,4,2}$), (d) near E-field for $k_0a = 2.0467460$ in the *xz*-plane ($WGMH_{1,3,2}$), (e) near E-field for $k_0a = 2.0590945$ in the *xz*-plane ($WGMH_{1,4,2}$), (f) BRCS for $k_0a = 2.0467460$ in the *xy*-plane ($WGMH_{1,3,2}$) and (g) BRCS for $k_0a = 2.0590945$ in the *xy*-plane ($WGMH_{1,4,2}$)

We believe that these results can be useful in the electromagnetic design of novel sensors, antennas and laser sources based on the dielectric disk cavities, in THz, infrared and visible light frequency ranges.

ACKNOWLEDGEMENTS

This work was supported in part by the Italian Ministry of University program 'Dipartimenti di Eccellenza 2018–2022' and by the National Research Foundation of Ukraine via the project No. 02-2020-0150.

ORCID

Mario Lucido https://orcid.org/0000-0001-8661-5601

REFERENCES

1. Fiedziuszko, S.J., Holme, S.: Dielectric resonators raise your high-Q. IEEE Microw. Mag. 2(3), 50–60 (2001)
2. Barannik, A., et al.: Whispering gallery mode resonators in microwave physics and technologies. Int. J. Microw. Wireless Technol. 9(4), 781–796 (2017)
3. Vitusevich, S.A., et al.: Design and characterization of an all-cryogenic low phase-noise sapphire K-band oscillator for satellite communication. IEEE Trans. Microw. Theor. Tech. 51(1), 163–169 (2003)
4. McCall, S.L., et al.: Whispering-gallery mode microdisk lasers. Appl. Phys. Lett. 60(3), 289–291 (1992)
5. He, L., Ozdemir, S.K., Yang, L.: Whispering gallery microcavity lasers. Laser Photon. Rev. 7(1), 60–82 (2013)
6. Zhang, Y., et al.: Advances in III-nitride semiconductor microdisk lasers. Phys. Status Solidi. 212(5), 960–973 (2015)
7. Fasching, G., et al.: Microcavity THz quantum cascade laser. Phys. E Low-Dimens. Syst. Nanostruct. 32(1,2), 316–319 (2006)
8. Lai, J., Greengard, L., O'Neil, M.: Robust integral formulations for electromagnetic scattering from three-dimensional cavities. J. Comput. Phys. 345, 1–16 (2017)
9. Lucido, M., Panariello, G., Schettino, F.: Scattering by polygonal cross-section dielectric cylinders at oblique incidence. IEEE Trans. Antenn. Propag. 58(2), 540–551 (2010)
10. Smotrova, E.I., et al.: Cold-cavity thresholds of microdisks with uniform and non-uniform gain: quasi-3D modeling with accurate 2D analysis. IEEE J. Sel. Top. Quant. Electron. 11(5), 1135–1142 (2005)
11. Balaban, M.V., et al.: Dual integral equations technique in electromagnetic wave scattering by a thin disk. Progr. Electromagn. Res. B. 16, 107–126 (2009)
12. Bleszynski, E., Bleszynski, M., Jaroszewicz, T.: Surface-integral equations for electromagnetic scattering from impenetrable and penetrable sheets. IEEE Antenn. Propag. Mag. 35, 14–24 (1993)
13. Nazarchuk, Z., Kobayashi, K.: Mathematical modelling of electromagnetic scattering from a thin penetrable target. Prog. Electromagn. Res. 55, 95–116 (2005)
14. Balaban, M.V., et al.: Accurate quantification of the Purcell effect in the presence of a microdisk of nanoscale thickness. IET Micro Nano Lett. 6(6), 393–396 (2011)
15. Shapoval, O.V., Sauleau, R., Nosich, A.I.: Scattering and absorption of waves by flat material strips analyzed using generalized boundary conditions and Nystrom-type algorithm. IEEE Trans. Antenn. Propag. 59(9), 3339–3346 (2011)
16. Sukharevsky, I.O., et al.: Validity and limitations of the median-line integral equation technique in the scattering by material strips of sub-wavelength thickness. IEEE Trans. Antenn. Propag. 62(7), 3623–3631 (2014)
17. Lucido, M.: Electromagnetic scattering by a perfectly conducting rectangular plate buried in a lossy half-space. IEEE Trans. Geosci. Rem. Sens. 52(10), 6368–6378 (2014)
18. Losada, V., Boix, R.R., Medina, F.: Fast and accurate algorithm for the short-pulse electromagnetic scattering from conducting circular plates buried inside a lossy dispersive halfspace. IEEE Trans. Geosci. Rem. Sens. 41, 988–997 (2003)
19. Lucido, M., Panariello, G., Schettino, F.: Scattering by a zero-thickness PEC disk: a new analytically regularizing procedure based on Helmholtz decomposition and Galerkin method. Radio Sci. 52(1), 2–14 (2017)
20. Lucido, M., Di Murro, F., Panariello, G.: Electromagnetic scattering from a zero-thickness PEC disk: a note on the Helmholtz-Galerkin analytically regularizing procedure. Progr. Electromagn. Res. Lett. 71, 7–13 (2017)
21. Lovat, G., et al.: Shielding of a perfectly conducting circular disk: exact and static analytical solution. Progr. Electromagn. Res. C. 95, 167–182 (2019)
22. Lucido, M., Migliore, M.D., Pinchera, D.: A new analytically regularizing method for the analysis of the scattering by a hollow finite-length PEC circular cylinder. Prog. Electromagn. Res. B. 70, 55–71 (2016)
23. Saidoglu, N.Y., Nosich, A.I.: Method of analytical regularization in the analysis of axially symmetric excitation of imperfect circular disk antennas. Comput. Math. Appl. 79(10), 2872–2884 (2020)
24. Lucido, M., Schettino, F., Panariello, G.: Scattering from a thin resistive disk: a guaranteed fast convergence technique. IEEE Trans. Antenn. Propag. 69(1), 387–396 (2021)
25. Lucido, M., et al.: A fast-converging scheme for the electromagnetic scattering from a thin dielectric disk. Electronics. 9(9), 1451 (2020)
26. Nosich, A.I.: Method of analytical regularization in computational photonics. Radio Sci. 51, 1421–1430 (2016)
27. Jones, D.S.: The Theory of Electromagnetism. Pergamon Press, New York (1964)
28. Abramowitz, M., Stegun, I.A.: Handbook of Mathematical Functions. Verlag Harri Deutsch, Frankfurt (1984)
29. Van Bladel, J.: A discussion of Helmholtz' theorem on a surface. Arch. Elekron. Üebertrag. 47(3), 131–136 (1993)
30. Wilkins, J.E.: Neumann series of Bessel functions. Trans. Amer. Math. Soc. 64, 359–385 (1948)
31. Van Bladel, J.: Electromagnetic Fields. IEEE Wiley, Hoboken, NJ (2007)
32. Titchmarsh, E.C.: Introduction to the Theory of Fourier Integrals. Oxford University Press, London (1948)
33. Gradstein, S., Ryzhik, I.M.: Tables of Integrals, Series and Products. Academin Press, New York (2000)
34. Krohns, S., et al.: Colossal dielectric constant up to gigahertz at room temperature. Appl. Phys. Lett. 94(12), 2903–2905 (2009)
35. Geng, N., Carin, L.: Wide-band electromagnetic scattering from a dielectric BOR buried in a layered lossy dispersive medium. IEEE Trans. Antenn. Propag. 47(4), 610–619 (1999)

How to cite this article: Lucido, M., Balaban, M.V., Nosich, A.I.: Plane wave scattering from thin dielectric disk in free space: generalized boundary conditions, regularizing Galerkin technique and whispering gallery mode resonances. IET Microw. Antennas Propag. 15(10), 1159–1170 (2021). https://doi.org/10.1049/mia2.12106

APPENDIX A

The Fredholm second-kind matrix equation obtained by means of the procedure detailed in Section 2 is:

$$\mathbf{x}_r^{(n)} + \mathbf{A}_r^{(n)}\mathbf{x}_r^{(n)} = \mathbf{b}_r^{(n)} \tag{A1}$$

where

$$\mathbf{A}_r^{(n)} = \begin{bmatrix} -\mathrm{j}\,2\omega\eta_r\mathbf{A}_{r,\mathrm{CC}}^{(n)} & -\mathrm{j}\,\sqrt{\dfrac{2\omega\eta_r}{-\mathrm{j}\,R_r}}\mathbf{A}_{r,\mathrm{CD}}^{(n)} \\ +\mathrm{j}\sqrt{\dfrac{2\omega\eta_r}{-\mathrm{j}\,R_r}}\mathbf{A}_{r,\mathrm{DC}}^{(n)} & -\dfrac{1}{R_r}\mathbf{A}_{r,\mathrm{DD}}^{(n)} \end{bmatrix} \tag{A2a}$$

$$\mathbf{x}_r^{(n)} = \begin{bmatrix} \dfrac{1}{\sqrt{2\omega\eta_r}}\mathbf{x}_{r,\mathrm{C}}^{(n)} \\ \sqrt{-\mathrm{j}\,R_r}\,\mathbf{x}_{r,\mathrm{D}}^{(n)} \end{bmatrix} \tag{A2b}$$

$$\mathbf{b}_r^{(n)} = \begin{bmatrix} -\mathrm{j}\,\sqrt{2\omega\eta_r}\mathbf{b}_{r,\mathrm{C}}^{(n)} \\ +\mathrm{j}\dfrac{1}{\sqrt{-\mathrm{j}\,R_r}}\mathbf{b}_{r,\mathrm{D}}^{(n)} \end{bmatrix} \tag{A2c}$$

$$\left(\mathbf{A}_{r,\mathrm{CC}}^{(n)}\right)_{-1,-1} = \left(\bar{\mathbf{A}}_{r,\mathrm{C}}^{(n)}\right)_{-1,-1} - (\alpha^{(n)})^2\left[\left(\bar{\mathbf{A}}_{r,\mathrm{D}}^{(n)}\right)_{-1,-1} - R_r\right] \tag{A2d}$$

for $n \neq 0$,

$$\left(\mathbf{A}_{r,\mathrm{CC}}^{(n)}\right)_{k,h} = \left(\mathbf{A}_{r,\mathrm{CC}}^{(n)}\right)_{h,k} = \left(\bar{\mathbf{A}}_{r,\mathrm{C}}^{(n)}\right)_{k,h} \tag{A2e}$$

for $k, h \geq -1 + \delta_{n,0}$ and $k + h \geq -1$,

$$\left(\mathbf{A}_{r,\mathrm{CD}}^{(n)}\right)_{-1,h} = \left(\mathbf{A}_{r,\mathrm{DC}}^{(n)}\right)_{h,-1}^{*} = -\alpha^{(n)}\left(\bar{\mathbf{A}}_{r,\mathrm{D}}^{(n)}\right)_{-1,h} \tag{A2f}$$

for $n \neq 0$ and $h \geq 0$,

$$\left(\mathbf{A}_{r,\mathrm{CD}}^{(n)}\right)_{k,h} = \left(\mathbf{A}_{r,\mathrm{DC}}^{(n)}\right)_{h,k} = 0 \tag{A2g}$$

$$\left(\mathbf{A}_{r,\mathrm{DD}}^{(n)}\right)_{k,h} = \left(\mathbf{A}_{r,\mathrm{DD}}^{(n)}\right)_{h,k} = \left(\bar{\mathbf{A}}_{r,\mathrm{D}}^{(n)}\right)_{k,h} \tag{A2h}$$

for $k, h \geq 0$, and

$$\left(\bar{\mathbf{A}}_{r,T}^{(n)}\right)_{k,h} = 2\sqrt{\eta_{T,k}^{(n)}\eta_{T,h}^{(n)}}\int_0^{+\infty}\tilde{K}_{r,T}(w)J_{\eta_{T,k}^{(n)}}(aw)J_{\eta_{T,h}^{(n)}}(aw)dw \tag{A2i}$$

$$\tilde{K}_{r,\mathrm{C}}(w) = \frac{\tilde{G}_{r,\mathrm{C}}(w) - R_r}{w^2} - \mathrm{j}\,\frac{1}{2\omega\eta_r w} \tag{A2j}$$

$$\tilde{K}_{r,\mathrm{D}}(w) = \frac{\tilde{G}_{r,\mathrm{D}}(w)}{w} \tag{A2k}$$

$$\alpha^{(n)} = \frac{\mathrm{j}\,\mathrm{sgn}(n)|n|!}{\Gamma(|n| + 3/2)}\sqrt{\frac{a(|n| + 1/2)}{2|n|}} \tag{A2l}$$

$$\left(\mathbf{x}_{r,\mathrm{C}}^{(n)}\right)_{-1} = \gamma_{r,\mathrm{C},-1}^{(n)} \tag{A2m}$$

for $n \neq 0$,

$$\left(\mathbf{x}_{r,T}^{(n)}\right)_h = \gamma_{r,T,h}^{(n)} \tag{A2n}$$

for $h \geq 0$,

$$\left(\mathbf{b}_{r,\mathrm{C}}^{(n)}\right)_{-1} = e^{\mathrm{j}\,n\phi_0}(-\mathrm{j})^{n+1}\left[\tilde{f}_{\mathrm{C}}^{(n,-1)}(k_\rho)F_{r0,\rho} - \alpha^{(n)}\tilde{f}_{\mathrm{D}}^{(n,-1)}(k_\rho)F_{r0,\phi}\right] \tag{A2o}$$

for $n \neq 0$,

$$\left(\mathbf{b}_{r,\mathrm{C}}^{(n)}\right)_k = e^{\mathrm{j}\,n\phi_0}(-\mathrm{j})^{n+1}\tilde{f}_{\mathrm{C}}^{(n,k)}(k_\rho)F_{r0,\rho} \tag{A2p}$$

$$\left(\mathbf{b}_{r,\mathrm{D}}^{(n)}\right)_k = e^{\mathrm{j}\,n\phi_0}(-\mathrm{j})^{n+1}\tilde{f}_{\mathrm{D}}^{(n,k)}(k_\rho)F_{r0,\phi} \tag{A2q}$$

for $k \geq 0$.

APPENDIX B

By means of Parseval's formula [32] and remembering Equation (10), it can be stated that:

$$\int_0^a \left|\underline{\mathbf{J}}_r^{(n)}(\rho)\right|^2\rho d\rho = \int_0^{+\infty}\left|\underline{\tilde{\mathbf{J}}}_r^{(n)}(w)\right|^2 wdw = \int_0^{+\infty}\left|\underline{\tilde{J}}_{r,\mathrm{C}}^{(n)}(w)\right|^2 wdw + \int_0^{+\infty}\left|\underline{\tilde{J}}_{r,\mathrm{D}}^{(n)}(w)\right|^2 wdw \tag{B1}$$

According to Equation (11), it is simple to write:

$$\int_0^{+\infty} \left|\tilde{J}_{r,T}^{(n)}(w)\right|^2 w dw = \sum_{h,h'=-1+\delta_{n,0}}^{+\infty} \gamma_{r,T,h}^{(n)} \left(\gamma_{r,T,h'}^{(n)}\right)^* I_{T,h,h'}^{(n)} \quad \text{(B2)}$$

where

$$I_{T,h,h'}^{(n)} = 2\sqrt{\eta_{T,h}^{(n)}\eta_{T,h'}^{(n)}} \int_0^{+\infty} J_{\eta_{T,h}^{(n)}}(aw) J_{\eta_{T,h'}^{(n)}}(aw) \frac{dw}{w^{2p_T-1}} \quad \text{(B3)}$$

To conclude, the integral in Equation (B3) can be written in closed form by using the Weber–Schafheitlin discontinuous integral [33], obtaining:

$$I_{T,h,h'}^{(n)} = \frac{\sqrt{\eta_{T,h}^{(n)}\eta_{T,h'}^{(n)}}(a/2)^{2p_T-2}\Gamma(2p_T-1)\Gamma(|n|+h+h'+2)}{\Gamma(-h+h'+p_T)\Gamma(|n|+h+h'+2p_T+1)\Gamma(h-h'+p_T)} \quad \text{(B4)}$$